ELSEVIER

Volume 182, Number 9, September 2009

JOURNAL OF SOLID STATE CHEMISTRY

www.elsevier.com/locate/jssc

CONTENTS

Abstracted/indexed in BioEngineering Abstracts, Chemical Abstracts, Coal Abstracts, Current Contents/Physics, Chemical, & Earth Sciences, Engineering Index, Research Alert, SCISEARCH, Science Abstracts, and Science Citation Index. Also covered in the abstract and citation database SCOPUS®. Full text available on ScienceDirect®.

Regular Articles

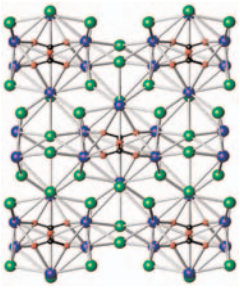

Ionothermal synthesis has provided single crystals of the mixed-anion material barium chloride carbonate, enabling the first determination of the complex crystal structure of this phase to be performed.

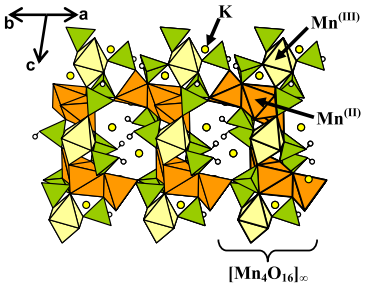

The three-dimensional intersecting tunnels structure of $K_3Mn^{II}_3Mn^{III}(PO_4)(H_{0.5}PO_4)_2(HPO_4)_2$ presents original $[Mn_4O_{16}]_\infty$ chains in which "$Mn^{II}_3O_{12}$" trimeric units alternate with $Mn^{III}O_6$ octahedra.

Regular Articles—Continued

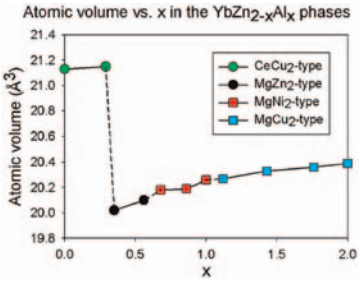

In the pseudobinary section $YbZn_{2-x}Al_x$ four structures occur in sequence on increasing the aluminium content: $CeCu_2$ (or KHg_2), $MgZn_2$, $MgNi_2$ and $MgCu_2$. Volumes per atom vs. composition are reported in the figure.

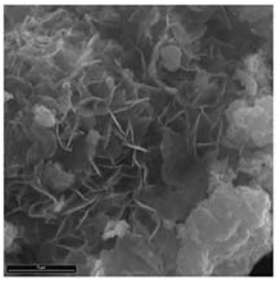

SEM micrograph (secondary electrons) of the synthesized Zn/Ni guarinoite showing that aggregates are composed of small plate-like particles.

Continued

Nuclear magnetic resonance study of Li and H diffusion in the high-temperature solid phase of $LiBH_4$

A.V. Soloninin, A.V. Skripov, A.L. Buzlukov and A.P. Stepanov

Page 2357

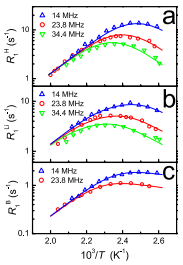

The measured spin–lattice relaxation rates of ^1H (a), ^7Li (b) and ^{11}B (c) as functions of the inverse temperature for the high-temperature solid phase of $LiBH_4$. The curves show the simultaneous Bloembergen–Purcell–Pound fits to the data with the fixed parameters of Li diffusion (the pre-exponential factor $\tau_0 = 1.1 \times 10^{-15}$ s and the activation energy $E_a = 0.56$ eV). This plot indicates that all the relaxation data for different nuclei and at different resonance frequencies are governed by a single Li jump process.

Liquid phase deposition synthesis of hexagonal molybdenum trioxide thin films

Shigehito Deki, Alexis Bienvenu Béléké, Yuki Kotani and Minoru Mizuhata

Page 2362

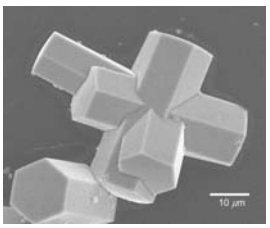

SEM photograph of typical h-$MoO_3.nH_2O$ thin film nuclei obtained after 36 h at 40 °C by the LPD method.

Strontium–copper selenite–chlorides: Synthesis and structural investigation

Peter S. Berdonosov, Andrei V. Olenev and Valery A. Dolgikh

Page 2368

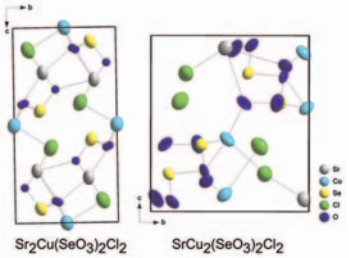

$Sr_2Cu(SeO_3)_2Cl_2$ and $SrCu_2(SeO_3)_2Cl_2$ were obtained and characterized by X-ray diffraction technique, DTA and IR spectroscopy.

The magnetic structure of clinopyroxene-type $LiFeGe_2O_6$ and revised data on multiferroic $LiFeSi_2O_6$

Günther J. Redhammer, Georg Roth, Werner Treutmann, Markus Hoelzel, Werner Paulus, Gilles André, Clemens Pietzonka and Georg Amthauer

Page 2374

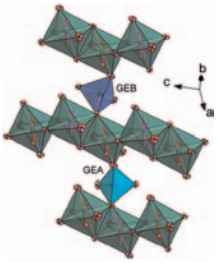

Section of the nuclear and magnetic structure of the synthetic clinopyroxene-type compound $LiFeGe_2O_6$ displaying the antiferromagnetic coupling of spins within the chains of $Fe^{3+}O_6$ octahedra and the antiferromagnetic (via Ge*B* sites) and ferromagnetic (via Ge*A* sites) coupling between these chains.

***In situ* X-ray diffraction study of reduction processes of Fe_3O_4- and $Fe_{1-x}O$-based ammonia-synthesis catalysts**

Yi-Fan Zheng, Hua-Zhang Liu, Zong-Jian Liu and Xiao-Nian Li

Page 2385

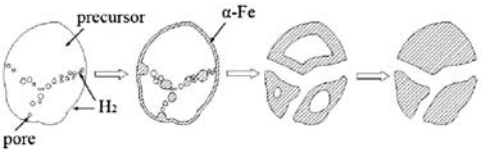

A proposed growth model of active phase α-Fe during reduction. Due to H_2 diffusing easily into the pores, reduction starts on outside and inside surface simultaneously to form "microcrystalline film", and the particles shrink during reduction which results in breaking of the aggregated oxide particle.

Organic carboxylate anions effect on the structures of a series of Mn(II) complexes based on 2-phenylimidazo [4,5-*f*]1,10-phenanthroline ligand

Xiuli Wang, Yongqiang Chen, Guocheng Liu, Hongyan Lin and Jinxia Zhang

Page 2392

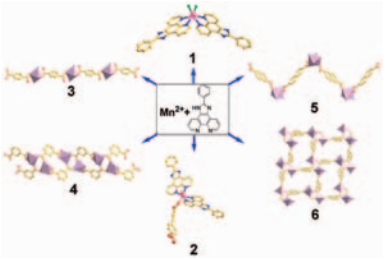

Through selecting organic carboxylate anions, six Mn(II) complexes have been synthesized under hydrothermal conditions and characterized by single crystal X-ray diffraction.

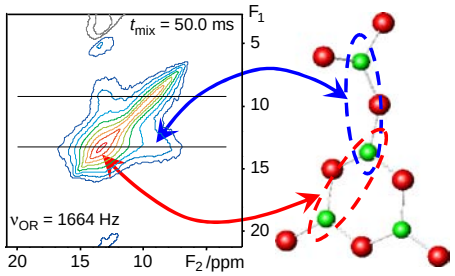

Connectivities and B–O–B bond angle distributions of ring and non-ring boron atoms in v-B_2O_3 have been determined by ^{11}B double rotation (DOR) NMR, multiple-quantum (MQ) DOR NMR and spin-diffusion DOR. Near-perfect planar, hexagonal [B_3O_6] boroxol rings are shown to be present.

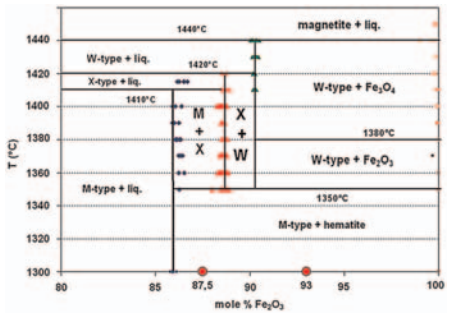

Part of the SrO–Fe_2O_3 phase diagram in air.

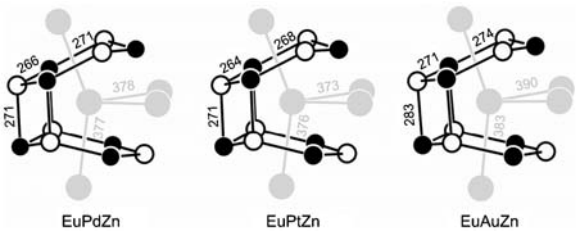

Europium coordination in EuPdZn, EuPtZn, and EuAuZn.

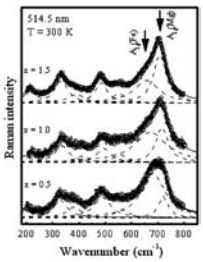

Raman spectra of $Mg_xFe_{3-x}O_4$ samples ($x = 0.5$, 1.0, and 1.5) using the Ar^+ 514.5 nm laser line.

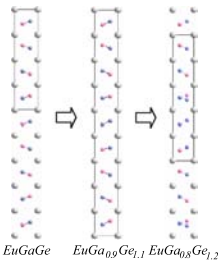

A study of Eu($Ga_{1-x}Si_x$)$_2$ and Eu($Ga_{1-x}Ge_x$)$_2$ shows different compositional ranges for puckering of 6^3 nets and, for the germanides, two new commensurately modulated superstructures.

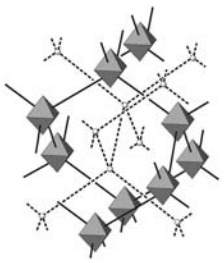

Two interpenetrating (pseudo)diamond nets formed by packing of the paramagnetic $[Ta_6Br_{12}(H_2O)]^{3+}$ (octahedral) and diamagnetic $[Et_4N]^+$ (spheres) cations.

Continued

On the crystal structures of Ln_3MO_7 (Ln = Nd, Sm, Y and M = Sb, Ta)—Rietveld refinement using X-ray powder diffraction data
W.T. Fu and D.J.W. IJdo
Page 2451

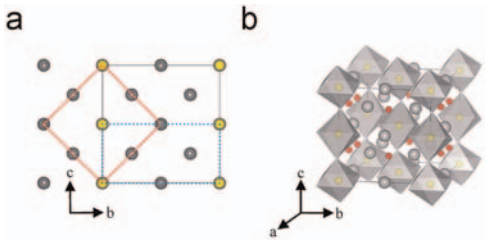

(a) A projected view of Ln_3MO_7 along the a-axis showing the ordering of Ln and M cations in the fluoride lattice. Note that the unit cells of the fluorite (dashed line), the parent $Cmmm$ (dashed line) and the $Cmcm/Ccmm$ structures (continuous line) are indicated. (b) Schematic representations of the crystal structures of Y_3SbO_7 showing SbO_6 octahedra and Y. Oxygens that do not bond to M cations are also shown.

Structure, crystal chemistry and thermal evolution of the δ-Bi_2O_3-related phase Bi_9ReO_{17}
Neeraj Sharma, Ray L. Withers, Kevin S. Knight and Chris D. Ling
Page 2468

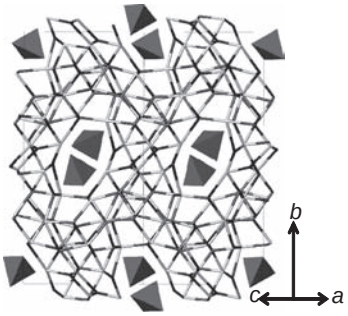

The crystal structure of Bi_9ReO_{17} viewed along the [101] direction. Bi atoms and bonds are light gray, O atoms and bonds are black and ReO_4 are represented by gray tetrahedra.

Preparation of iron oxides using ammonium iron citrate precursor: Thin films and nanoparticles
Sangmoon Park
Page 2456

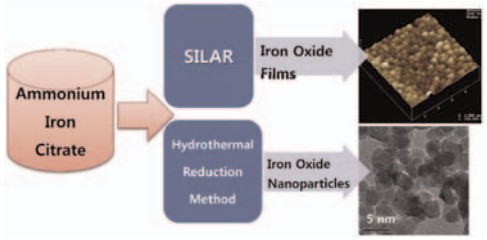

Both iron-oxide thin films and nanoparticles (about 4 nm in diameter) are successfully achieved via successive-ionic-layer-adsorption-and-reaction and hydrothermal techniques in the use of ammonium iron citrate as a precursor.

General and facile synthesis of ceria-based solid solution nanocrystals and their catalytic properties
Huan-Ping Zhou, Rui Si, Wei-Guo Song and Chun-Hua Yan
Page 2475

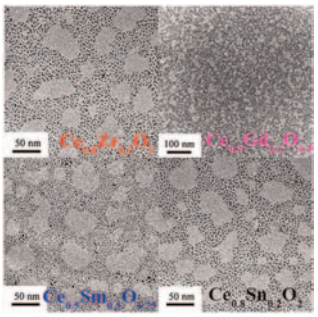

Uniform ultra-small nanostructured $Ce_{1-x}Zr_xO_2$, $Ce_{1-x}Gd_xO_{1-x/2}$, $Ce_{1-x}Sm_xO_{1-x/2}$, and $Ce_{1-x}Sn_xO_2$ solid solutions with homogeneous textures were synthesized through a thermolysis process, facilitated by the initial formation of precursors (hydrated (Ce,M)-hydroxides).

$PbMn(SO_4)_2$: A new chiral antiferromagnet
D.V. West, I.D. Posen, Q. Huang, H.W. Zandbergen, T.M. McQueen and R.J. Cava
Page 2461

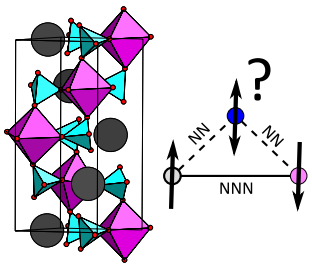

$PbMn(SO_4)_2$ crystallizes with chiral symmetry, forming a double-helical arrangement of Pb^{2+} and Mn^{2+} cations. It orders antiferromagnetically at 5.5 K and shows signs of magnetic frustration.

Fabrication of a graphene–cuprous oxide composite
Chao Xu, Xin Wang, Lichun Yang and Yuping Wu
Page 2486

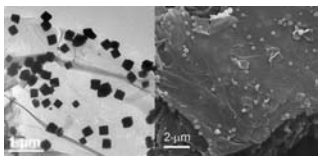

The graphene oxide sheets are reduced and almost exfoliated due to the in-situ formation of Cu_2O crystals deriving from the adsorbed copper acetate.

Synthesis, structure and magnetic behavior of a new three-dimensional Manganese phosphite-oxalate: $[C_2N_2H_{10}][Mn_2^{II}(OH_2)_2(HPO_3)_2(C_2O_4)]$

Padmini Ramaswamy, Sukhendu Mandal and Srinivasan Natarajan

Page 2491

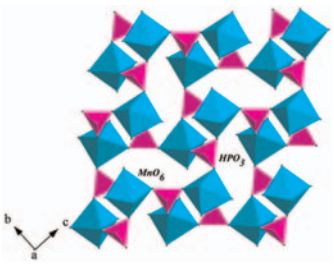

A new antiferromagnetic three-dimensional inorganic–organic hybrid compound, $[C_2N_2H_{10}][Mn_2^{II}(OH_2)_2(HPO_3)_2(C_2O_4)]$ has been prepared hydrothermally. The compound has neutral manganese layers pillared by oxalate units. The neutral manganese layers are shown here.

The ternary system cerium–palladium–silicon

Alexey Lipatov, Alexander Gribanov, Andriy Grytsiv, Peter Rogl, Elena Murashova, Yurii Seropegin, Gerald Giester and Konstantin Kalmykov

Page 2497

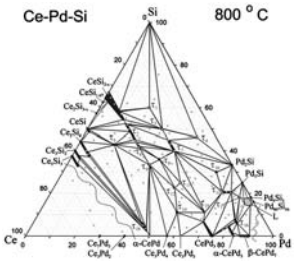

Phase relations in the ternary system Ce–Pd–Si have been established for the isothermal section at 800 °C based on X-ray powder diffraction, metallography, SEM and EMPA techniques on about 130 alloys. 18 ternary compounds were observed.

Uniform AMoO$_4$:Ln (A = Sr^{2+}, Ba^{2+}; Ln = Eu^{3+}, Tb^{3+}) submicron particles: Solvothermal synthesis and luminescent properties

Piaoping Yang, Chunxia Li, Wenxin Wang, Zewei Quan, Shili Gai and Jun Lin

Page 2510

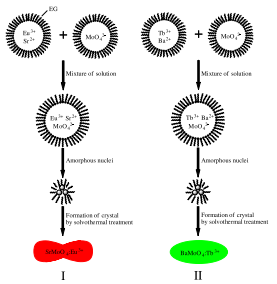

Uniform rare-earth ions (Eu^{3+}, Tb^{3+}) doped AMoO$_4$ (A = Sr, Ba) submicron phosphors with tetragonal scheelite-type structure have been prepared through a facile solvothermal process using EG as reaction media.

Preparation and photocatalytic ability of highly defective carbon nanotubes

Yongsong Luo, Yaofu Heng, Xiaojun Dai, Wenquan Chen and Jialin Li

Page 2521

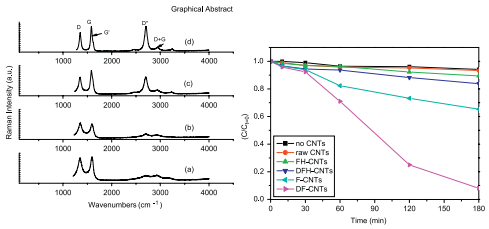

The highly defective carbon nanotubes (CNTs) were prepared using a heat-treatment technique. The results showed that the highly defective CNTs had the photocatalytic ability in the range of visible light.

Magnetic properties of $Co_2V_2O_7$ single crystals grown by flux method

Zhangzhen He, Jun-Ichi Yamaura, Yutaka Ueda and Wendan Cheng

Page 2526

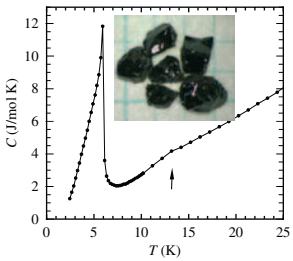

Single crystals of $Co_2V_2O_7$ are grown using V_2O_5 as self-flux at a slow cooling rate. Magnetic properties are investigated by means of susceptibility, magnetization, and heat capacity measurements, showing that $Co_2V_2O_7$ is likely to be a three-dimensional antiferromagnet with two magnetic transitions at low temperature.

Synthesis of sulfated titania supported on mesoporous silica using direct impregnation and its application in esterification of acetic acid and *n*-butanol

Yuhong Wang, Yunting Gan, Roger Whiting and Guanzhong Lu

Page 2530

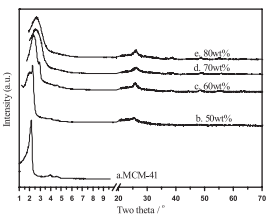

XRD profiles of the composites of S-TiO_2/MCM-41 with different TiO_2 contents. The low angle peaks indicate the MCM-41-like structure retained and a TiO_2 phase appeared at high angle region.

Continued

Pressure-induced structural transformations of the Zintl phase sodium silicide

Raúl Quesada Cabrera, Ashkan Salamat, Oleg I. Barkalov, Olivier Leynaud, Peter Hutchins, Dominik Daisenberger, Denis Machon, Andrea Sella, Dewi W. Lewis and Paul F. McMillan

Page 2535

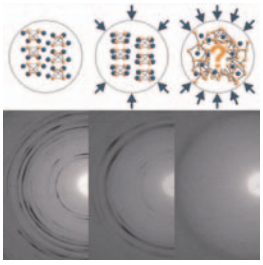

The high-pressure behaviour of NaSi has been studied using Raman spectroscopy and angle-dispersive synchrotron X-ray diffraction. Our studies reveal a first structural transformation occurring at 8–10 GPa, followed by irreversible amorphisation, suggesting the formation of Si–Si bonds with oxidation of the Si^{-} species and reduction of Na^{+} to metallic sodium. We have combined our experimental studies with DFT calculations to assist in the analysis of the structural behaviour of NaSi at high pressure.

Soft ferromagnet $GdFe_{7.7}Si_{1.3}$ with a $CaCu_5$-to-$Th_2(Ni/Zn)_{17}$ transitional structure

Volodymyr Svitlyk, Yan Yin Janice Cheung and Yurij Mozharivskyj

Page 2543

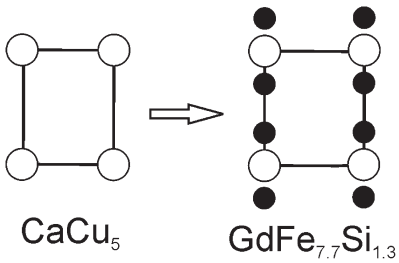

The basic structure of the soft ferromagnet $GdFe_{7.7}Si_{1.3}$ is derived from that of $CaCu_5$ through random substitution of Gd atoms by Fe_2 dumbbells.

Neutron diffraction study of the β' and γ phases of $LiFeO_2$

Maud Barré and Michele Catti

Page 2549

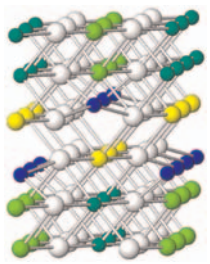

Crystal structure of β'-$LiFeO_2$ (monoclinic $C2/c$). Lithium and iron atoms are both ordered (blue and yellow balls) and partially disordered (green balls) over four independent sites. The β' phase transforms to fully ordered γ (tetragonal $I4_1/amd$) at 550 °C.

Solvent-dependent luminescent Cu(I) framework based on 5-(4-pyridyl)tetrazole

Fei Wang, Rongmin Yu, Qi-Sheng Zhang, Zhen-Guo Zhao, Xiao-Yuan Wu, Yi-Ming Xie, Li Qin, Shan-Ci Chen and Can-Zhong Lu

Page 2555

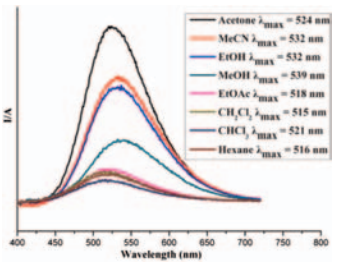

A new Cu(I) compound, $Cu_4(L)_4 \cdot 2EtOH$ (**1**) (L = 5-(4-pyridyl) tetrazole), was synthesized under solvothermal method, which displays an interesting solvent-dependent luminescence.

Pulsed laser-induced oxygen deficiency at TiO_2 surface: Anomalous structure and electrical transport properties

Tomohiko Nakajima, Tetsuo Tsuchiya and Toshiya Kumagai

Page 2560

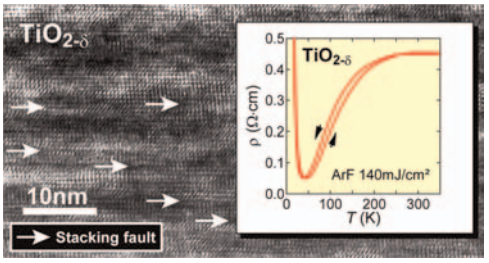

A pulsed laser-irradiated $TiO_{2-\delta}$ substrate showed an unconventional metallic phase, with hysteresis over a wide range of temperatures and a metal–insulator transition at 42 K.

Effect of added zinc on the properties of cobalt-containing ceramic pigments prepared from layered double hydroxides

M.E. Pérez-Bernal, R.J. Ruano-Casero and V. Rives

Page 2566

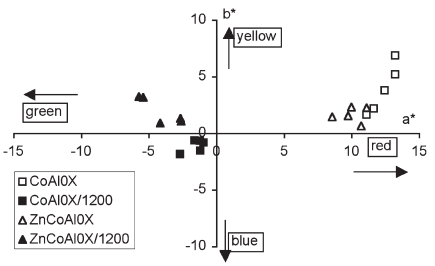

Mixed oxides from layered double hydroxides (LDHs) with the hydrotalcite-type structure containing Co and Al or Zn, Co and Al in the brucite-like layers are potential candidates for ceramic pigments with tunable colour properties.

Effects of Mn substitution on the structure and properties of chalcopyrite-type $CuInSe_2$
Jinlei Yao, Carly N. Kline, Hao Gu, Mi Yan and Jennifer A. Aitken
Page 2579

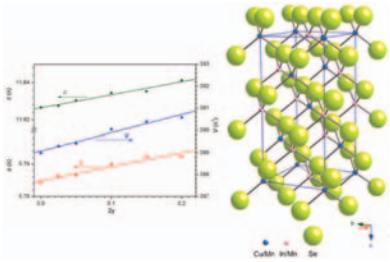

The manganese solid solubility can reach up to 10% and 20% for $CuIn_{1-x}Mn_xSe_2$ and $Cu_{1-y}In_{1-y}Mn_{2y}Se_2$, respectively, while maintaining phase-pure, chalcopyrite-type materials. Lattice parameters increase linearly with increase manganese concentration suggesting that the manganese ions are distributed randomly on both the indium site and the copper and indium sites simultaneously.

$RbAuUSe_3$, $CsAuUSe_3$, $RbAuUTe_3$, and $CsAuUTe_3$: Syntheses and structure; magnetic properties of $RbAuUSe_3$
Daniel E. Bugaris and James A. Ibers
Page 2587

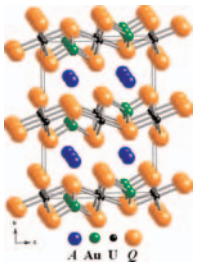

View down [100] of the crystal structure of the isostructural AAuUQ3 (A=Rb, Cs; Q=Se, Te) compounds.